Rapid quantitative phase imaging for partially coherent light microscopy

José A. Rodrigo[1,*] and Tatiana Alieva[1]

[1]*Universidad Complutense de Madrid, Facultad de Ciencias Físicas, Ciudad Universitaria s/n, Madrid 28040, Spain*

[*]jarmar@fis.ucm.es

Abstract: Partially coherent light provides promising advantages for imaging applications. In contrast to its completely coherent counterpart, it prevents image degradation due to speckle noise and decreases cross-talk among the imaged objects. These facts make attractive the partially coherent illumination for accurate quantitative imaging in microscopy. In this work, we present a non-interferometric technique and system for quantitative phase imaging with simultaneous determination of the spatial coherence properties of the sample illumination. Its performance is experimentally demonstrated in several examples underlining the benefits of partial coherence for practical imagining applications. The programmable optical setup comprises an electrically tunable lens and sCMOS camera that allows for high-speed measurement in the millisecond range.

OCIS codes: (100.3010) Image reconstruction techniques; (030.0030) Coherence and statistical optics; (100.5070) Phase retrieval; (110.0180) Microscopy; (120.4630) Optical inspection; (120.5050) Phase measurement.

References

1. F. Charrière, A. Marian, F. Montfort, J. Kuehn, T. Colomb, E. Cuche, P. Marquet, and C. Depeursinge, "Cell refractive index tomography by digital holographic microscopy," Opt. Lett. **31**, 178–180 (2006).
2. Y. Sung, W. Choi, C. Fang-Yen, K. Badizadegan, R. R. Dasari, and M. S. Feld, "Optical diffraction tomography for high resolution live cell imaging," Opt. Express **17**, 266–277 (2009).
3. M. Kim, *Digital Holographic Microscopy: Principles, Techniques, and Applications*, Springer Series in Optical Sciences (Springer, 2011).
4. P. Ferraro, A. Wax, and Z. Zalevsky, *Coherent Light Microscopy: Imaging and Quantitative Phase Analysis*, Springer Series in Surface Sciences (Springer, 2011).
5. Y. Cotte, F. Toy, P. Jourdain, N. Pavillon, D. Boss, P. Magistretti, P. Marquet, and C. Depeursinge, "Marker-free phase nanoscopy," Nat Photon **7**, 113–117 (2013).
6. R. W. Gerchberg and W. O. Saxton, "A practical algorithm for the determination of phase from image and diffraction plane pictures," Optik **35**, 237–246 (1972).
7. L. Camacho, V. Micó, Z. Zalevsky, and J. García, "Quantitative phase microscopy using defocusing by means of a spatial light modulator," Opt. Express **18**, 6755–6766 (2010).
8. J. A. Rodrigo, T. Alieva, G. Cristóbal, and M. L. Calvo, "Wavefield imaging via iterative retrieval based on phase modulation diversity," Opt. Express **19**, 18621–18635 (2011).
9. T. E. Gureyev and K. A. Nugent, "Rapid quantitative phase imaging using the transport of intensity equation," Opt. Commun. **133**, 339–346 (1997).
10. C. Zuo, Q. Chen, W. Qu, and A. Asundi, "High-speed transport-of-intensity phase microscopy with an electrically tunable lens," Opt. Express **21**, 24060–24075 (2013).
11. Y. Park, M. Diez-Silva, G. Popescu, G. Lykotrafitis, W. Choi, M. S. Feld, and S. Suresh, "Refractive index maps and membrane dynamics of human red blood cells parasitized by plasmodium falciparum," PNAS **105**, 13730–13735 (2008).

12. B. Rappaz, A. Barbul, Y. Emery, R. Korenstein, C. Depeursinge, P. J. Magistretti, and P. Marquet, "Comparative study of human erythrocytes by digital holographic microscopy, confocal microscopy, and impedance volume analyzer," Cytometry Part A **73A**, 895–903 (2008).
13. B. Redding, M. A.Choma, and H. Cao, "Speckle-free laser imaging using random laser illumination," Nat Photonics **6**, 355–359 (2012).
14. M. Nixon, B. Redding, A. A. Friesem, H. Cao, and N. Davidson, "Efficient method for controlling the spatial coherence of a laser," Opt. Lett. **38**, 3858–3861 (2013).
15. B. Kemper, S. Sturwald, C. Remmersmann, P. Langehanenberg, and G. von Bally, "Characterisation of light emitting diodes (LEDs) for application in digital holographic microscopy for inspection of micro and nanostructured surfaces," Opt. Lasers Eng. **46**, 499–507 (2008).
16. P. Langehanenberg, G. v. Bally, and B. Kemper, "Application of partially coherent light in live cell imaging with digital holographic microscopy," J. Mod. Opt. **57**, 709–717 (2010).
17. S. O. Isikman, W. Bishara, and A. Ozcan, "Partially coherent lensfree tomographic microscopy [Invited]," Appl. Opt. **50**, H253–H264 (2011).
18. T. Kim, R. Zhou, M. Mir, S. D. Babacan, P. S. Carney, L. L. Goddard, and G. Popescu, "White-light diffraction tomography of unlabelled live cells," Nat Photonics **8**, 256–263 (2014).
19. J. W. Goodman, *Statistical Optics* (Wiley&Sons, 2000).
20. I. Abdulhalim, "Spatial and temporal coherence effects in interference microscopy and full-field optical coherence tomography," Ann. Phys-Berlin **524**, 787–804 (2012).
21. A. C. Schell, "The multiple plate antenna," Ph.D. thesis, Massachusetts Institute of Technology (1961).
22. C. Minetti, N. Callens, G. Coupier, T. Podgorski, and F. Dubois, "Fast measurements of concentration profiles inside deformable objects in microflows with reduced spatial coherence digital holography," Appl. Opt. **47**, 5305–5314 (2008).
23. T. J. McIntyre, C. Maurer, S. Fassl, S. Khan, S. Bernet, and M. Ritsch-Marte, "Quantitative SLM-based differential interference contrast imaging," Opt. Express **18**, 14063–14078 (2010).
24. J. A. Rodrigo and T. Alieva, "Recovery of Schell-model partially coherent beams," Opt. Lett. **39**, 1030–1033 (2014).
25. F. O. Fahrbach, F. F. Voigt, B. Schmid, F. Helmchen, and J. Huisken, "Rapid 3D light-sheet microscopy with a tunable lens," Opt. Express **21**, 21010–21026 (2013).
26. J. Clark, X. Huang, R. Harder, and I. Robinson, "High-resolution three-dimensional partially coherent diffraction imaging," Nat Commun **3**, 993 (2012).
27. D. Mendlovic, Z. Zalevsky, and N. Konforti, "Computation considerations and fast algorithms for calculating the diffraction integral," J. Mod. Optic **44**, 407–414 (1997).
28. M. A. Herráez, D. R. Burton, M. J. Lalor, and M. A. Gdeisat, "Fast two-dimensional phase-unwrapping algorithm based on sorting by reliability following a noncontinuous path," Appl. Opt. **41**, 7437–7444 (2002).
29. A. V. Martin, F. R. Che, W. K. Hsieh, J. J. Kai, S. D. Findlay, and L. J. Allen, "Spatial incoherence in phase retrieval based on focus variation," Ultramicroscopy **106**, 914–924 (2006).
30. J. W. Goodman, *Introduction to Fourier Optics,* (Roberts&Company, 2005).

1. Introduction

Coherent light is extensively applied in numerous imaging techniques. In particular, digital holographic microscopy is a well-established interferometric technique that exploits the high coherence of laser beams to reconstruct the phase information of the light scattered by the object [1–5]. Phase-shifting holographic techniques, which require the measurement of several interference patterns, have been developed for high-resolution topography analysis of the object with an axial resolution up to nanometer range [3, 5]. Alternatively, non-interferometric techniques based on the measurement few diffraction patterns have also been successfully applied for quantitative phase imaging. They comprise iterative phase retrieval algorithms [6–8], or non-iterative methods that solve the so-called transport of intensity equation (TIE) [9, 10]. All these computational imaging techniques allow for marker-free live cell analysis, which is highly demanded in biomedical sciences [10–12].

The main drawbacks of coherent laser-based imaging are the speckle noise and distortions caused by parasitic reflections in the optical setup and the sample's chamber itself. Speckle noise, associated to multiple scattering arsing from cell clusters layered in biofilms or other scattering media, decreases both the accuracy and signal-to-noise ratio of the reconstructed phase images. Moreover, the image obtained under highly coherent illumination suffers from

cross-talk caused by objects located in the same or surrounding depth layers comprising the sample.

Temporal and spatial partially coherent light can be used to overcome such drawbacks, see for example [13, 14]. In the case of low coherent sources the beams scattered by objects separated by more than the coherence length do not interfere each other at the detection plane. This coherence gating effect allows for depth discrimination (optical sectioning) and therefore is useful for cross-talk reduction. In addition, the partial coherence mitigates speckle noise. Recently, low coherent light sources such as halogen lamps or light emission diodes (LEDs) have also been applied in digital holographic microscopy, [15–18]. For instance, in [15, 16] the noise reduction in the reconstructed phase has been experimentally demonstrated for LED illumination. Nevertheless, off-axis digital holographic microscopy is difficult to implement with a coherent length of only few microns. In this case both interferometer arms have to be accurately compensated, for example, by equal glass-based optical components in order to optimize the contrast of the holograms.

The description of optical imaging with temporal and spatial partially coherent light is inherently complex and requires the consideration of the complex mutual coherence function. In the stationary quasi-monochromatic case, which is often fulfilled for color LED sources, it can be written as a product of temporal and spatial coherence functions $J(\tau)\Gamma(\mathbf{r}_1,\mathbf{r}_2)$ [19]. The temporal function $J(\tau)$ describes the coherence gating effect often exploited for axial optical sectioning [20]. According to the Wiener-Khinchin theorem, it corresponds to the Fourier transform of the source power spectrum. In the case of quasi-monochromatic LED source ($\Delta\lambda \ll \lambda_0$) with nearly Gaussian spectrum, the coherence length is often approximated as $l_c \approx 0.88\lambda_0^2/\Delta\lambda$ where λ_0 is the central wavelength and $\Delta\lambda$ is the full width at half maximum (FWHM) of the spectrum [19].

On the other hand, the spatial coherence function $\Gamma(\mathbf{r}_1,\mathbf{r}_2)$, referred to as mutual intensity (MI), describes the image formation of a sample's layer. In the scalar paraxial approximation the MI of a two-dimensional (2D) wavefield is described by a complex-valued 4D MI defined as $\Gamma(\mathbf{r}_1,\mathbf{r}_2) = \langle f(\mathbf{r}_1) f^*(\mathbf{r}_2)\rangle$, where: $\mathbf{r}_{1,2} = (x,y)_{1,2}$ is a position vector in a plane transverse to the light propagation direction and $\langle \cdot \rangle$ stands for ensemble averaging. Completely coherent beams are characterized by $\Gamma_c(\mathbf{r}_1,\mathbf{r}_2) = f(\mathbf{r}_1) f^*(\mathbf{r}_2)$ while Schell-model partially coherent beams (SMBs) [21] are described by $\Gamma(\mathbf{r}_1,\mathbf{r}_2) = f(\mathbf{r}_1) f^*(\mathbf{r}_2) \gamma(\mathbf{r}_1 - \mathbf{r}_2) = \Gamma_c(\mathbf{r}_1,\mathbf{r}_2)\gamma(\triangle\mathbf{r})$, where $\gamma(\triangle\mathbf{r})$ is an equal-time complex degree of spatial coherence (DSC). The Schell model is widely used in different imaging applications, including microscopy. For instance, in bright field microscopes under Köhler illumination with incoherent source, the SMB corresponds to the beam scattered by an object described by the complex modulation function $f(\mathbf{r})$. In this case the DSC, $\gamma(\triangle\mathbf{r})$, at the sample plane is given by the Fourier transform of the intensity distribution of the illumination beam in the condenser lens aperture, according to the van-Cittert-Zernike theorem [19]. Therefore, the SMB is present in illumination schemes with different sources such as LEDs, halogen lamps and randomized laser beams, however, its experimental characterization is challenging. The DSC can be tuned in several ways, for example, by spatial filtering of the incoherent source or by using a moving diffuser in the case of a coherent source (e.g. laser) [22–24]. We underline that a pinhole of few microns (e.g. 25 μm) is often used as a spatial filter for LED and halogen sources in order to obtain high spatial coherence but low temporal coherence [15–18]. In contrast, we consider quantitative phase imaging with an illumination light exhibiting significantly reduced spatial and temporal coherence.

In this work, we present a non-interferometric technique and optical system for fast quantitative phase imaging of objects under quasi-monochromatic partially coherent illumination. The technique allows for in-situ reconstruction of both the object wavefield $f(\mathbf{r})$ and the DSC of the illumination beam. Its performance is experimentally demonstrated in several examples

which underline the advantages of partial coherent light for speckle-noise and cross-talk reduction. The reconstructed object wavefield can be numerically refocused for accurate topography analysis or inspection of the sample. The proposed experimental setup comprises a high-speed sCMOS camera and electrically tunable fluidic lens (ETL), which focal length is tuned in few milliseconds by applying current control. In contrast to the widely used liquid-crystal spatial light modulators, the ETLs have faster response. In addition, they are made from low dispersion and polarization preserving materials. Such ETLs have been used for high-speed volumetric imaging [25] and phase retrieval of coherent beams [10].

2. Principle of the MI recovery technique

In conventional optical microscopes the image of the object can be acquired by a digital camera placed at the back focal plane of the tube lens. The proposed technique is able to reconstruct both the object wavefield and the DSC of the illumination beam (MI recovery) at this imaging plane. It requires the measurement of several intensity distributions (at least four) of the beam transformed by an optical system comprising a relay lens (RL) and the ETL. The input plane of this system coincides with the imaging plane of the microscope and the digital camera is fixed at distance d from the ETL as sketched in Fig. 1(a). Therefore, the input beam is focused into the ETL and then imaged into the detector plane (e.g. sCMOS camera) for several values of the ETL's focal length: f_m. This measurement setup can be easily attached to the microscope as sketched in Fig. 1(b). We underline that the tube lens and RL are identical.

For Schell-model input beams (as in Section 1), the intensity distribution at the detector plane of the system [Fig. 1(a)] is given by the expression

$$I_{PC}^{(m)}(\mathbf{r}_o) = I_C^{(m)}(\mathbf{r}_o) \otimes \widetilde{\gamma}_m(\mathbf{r}_o) = \int I_C^{(m)}(\mathbf{r}'_o) \widetilde{\gamma}_m(\mathbf{r}_o - \mathbf{r}'_o) \, d\mathbf{r}'_o, \tag{1}$$

where $\widetilde{\gamma}_m(\mathbf{r}_o)$ is the scaled Fourier transform (FT) of the input DSC: $\widetilde{\gamma}_m(\mathbf{r}_o) = FT[\gamma(\mathbf{r})](\mathbf{r}_o S_m)$ with $S_m = f_m/(d - f_m)$ being the scaling factor, see Appendix. Note that $FT[\cdot]$ indicates the FT optically performed by the RL. The expression Eq. (1) is the convolution between the *coherent intensity* $I_C^{(m)}(\mathbf{r}_o) = |\mathscr{F}^{(m)}[f(\mathbf{r})](\mathbf{r}_o)|^2$ and the function $\widetilde{\gamma}_m(\mathbf{r}_o)$, where $\mathscr{F}^{(m)}$ describes the propagation of $f(\mathbf{r})$ through the system (see Appendix). This makes possible the MI recovery of SMBs as it was experimentally demonstrated in [24] for a similar optical system. Here, we adapt the iterative algorithm developed in [24] for MI recovery to this particular case.

The iterative algorithm sketched in Fig. 1(c) reconstructs the wavefield $g(\mathbf{r}_i)$ at the input of the ETL by using the measured intensities $I_{PC}^{(m)}(\mathbf{r}_o)$ as constraint images. This wavefield is back propagated to the system's input plane to obtain the object function: $f(\mathbf{r}) = FT[g(\mathbf{r}_i)](\mathbf{r})$. Specifically, the iterative algorithm comprises two loops labeled with index $m = 1, \ldots, M$ and $n = 1, \ldots, N$, where M is the number of measurements and $M \times N$ is the total number of iterations. The wavefield at the detector plane is $W_{m,n}(\mathbf{r}_o) = F_d[g_n(\mathbf{r}_i)L_m(\mathbf{r}_i)](\mathbf{r}_o)$:

$$W_{m,n}(\mathbf{r}_o) = \frac{\exp(i2\pi d/\lambda_0)}{i\lambda_0 d} \int g_n(\mathbf{r}_i) L_m(\mathbf{r}_i) \exp\left(i\pi \frac{(\mathbf{r}_o - \mathbf{r}_i)^2}{\lambda_0 d}\right) d\mathbf{r}_i, \tag{2}$$

corresponding to the Fresnel diffraction integral of the current wavefield estimate $g_n(\mathbf{r}_i)$, where $L_m(\mathbf{r}_i) = \exp\left(-i\pi \mathbf{r}_i^2/\lambda_0 f_m\right)$ is the transmission function of the ETL. This approximation of the ETL is justified in the Appendix and has also been assumed in other ETL-based setups, see for example [10, 25]. For a realistic initial estimate of the input beam a circle function $\mathrm{circ}(2|\mathbf{r}|/D)$ (in our case with diameter $D = 5$ mm) can be considered, thus it yields $g_1(\mathbf{r}_i) = FT[\mathrm{circ}(2|\mathbf{r}|/D)](\mathbf{r}_i)$. The whole iterative process is described as it follows: (*i*) A new estimate
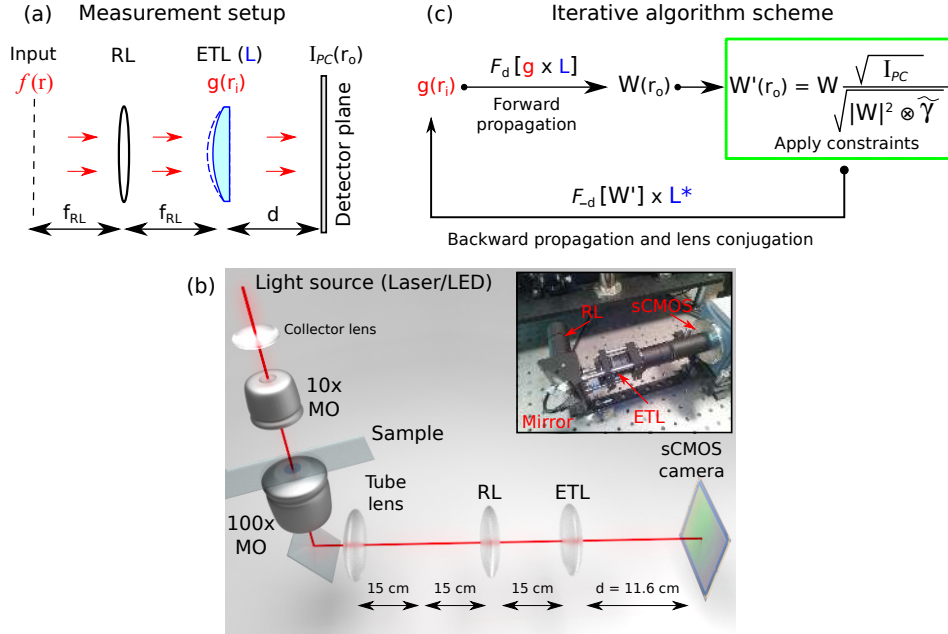
Fig. 1. (a) Setup for the measurement of constraint images $I_{PC}(\mathbf{r}_o)$. This setup is attached to the microscope as sketched in (b). Collector lens projects the illumination beam (laser or LED) into the condenser ($10\times$ MO). The sample is imaged by the objective lens ($100\times$ MO) and tube lens, which is identical to the relay lens (RL) with focal length of 15 cm. Inset displays the measurement device: ETL (Optotune, EL-10-30-C) and high-speed sCMOS camera (Hamamatsu, Orca Flash 4.0). (c) Scheme of the iterative MI recovery algorithm.

of $W_{m,n}(\mathbf{r}_o)$ is obtained from the current version of $g_n(\mathbf{r}_i)$, and then is replaced by the updated version

$$W'_{m,n}(\mathbf{r}_o) = W_{m,n}(\mathbf{r}_o)\sqrt{I_{PC}^{(m)}(\mathbf{r}_o)}/\sqrt{\Im_{PC}^{(m,n)}(\mathbf{r}_o)}, \qquad (3)$$

where the current estimate of the intensity is $\Im_{PC}^{(m,n)}(\mathbf{r}_o) = \Im_C^{(m,n)}(\mathbf{r}_o) \otimes \widetilde{\gamma}_m(\mathbf{r}_o)$, being $\Im_C^{(m,n)}(\mathbf{r}_o) = |W_{m,n}(\mathbf{r}_o)|^2$; (ii) Then, the wavefield Eq. (3) is back-propagated to the ETL input plane obtaining a new estimate of the wavefield $g_n(\mathbf{r}_i) = F_{-d}[W'_{m,n}(\mathbf{r}_o)] \times L_m^*(\mathbf{r}_i)$, where * denotes complex conjugation. The next estimate of $W_{m+1,n}(\mathbf{r}_o)$ is transformed into $W'_{m+1,n}(\mathbf{r}_o)$; (iii) the procedure described in (ii) is performed using the rest of measured intensities, until $m = M$. Then $W'_{M,n}(\mathbf{r}_o)$ is inverted to obtain an updated estimate of the wavefield: $g_{n+1}(\mathbf{r}_i) = F_{-d}[W'_{M,n}(\mathbf{r}_o)] \times L_M^*(\mathbf{r}_i)$; The process (i)-(iii) is iterated over the index n and stops (at $n = N$) when the estimated intensities $\Im_{PC}^{(m,N)}(\mathbf{r}_o)$ coincide with the measured ones or when algorithm convergence is reached. Note that in the completely coherent case, $\widetilde{\gamma}_m(\mathbf{r}_o) \rightarrow \delta(\mathbf{r}_o - \mathbf{r}'_o)$, expression Eq. (3) reduces to the usual modulus constraint that replaces the amplitude by the measured one while retaining the phase.

In numerous practical applications the DSC of the illumination beam is unknown and difficult to determine. The proposed algorithm can also estimate the DSC, which results crucial to reconstruct the object wavefield. This requires an additional routine in the algorithm for the DSC determination, as for example the Richardson-Lucy deconvolution (RLD) reported in [26] for the Fourier transform and generalized in [24] for more complex transformations and systems.

Here, the RLD is performed in each iteration step (i) as it follows:

$$\widetilde{\gamma}_m^{(k+1)}(\mathbf{r}_o) = \widetilde{\gamma}_m^{(k)}(\mathbf{r}_o) \times \left(P^{(m,n)}(-\mathbf{r}_o) \otimes \frac{I_{PC}^{(m)}(\mathbf{r}_o)}{P^{(m,n)}(\mathbf{r}_o) \otimes \widetilde{\gamma}_m^{(k)}(\mathbf{r}_o)} \right), \qquad (4)$$

with $k = 1, \ldots, K$ being the RLD iteration index, where $P^{(m,n)}(\mathbf{r}_o) = 2\Im_C^{(m,n)} - \Im_C^{(m,n-1)}$ is a combination of the current and previous estimate of the coherent intensity. As initial estimate $\widetilde{\gamma}_m^{(1)}(\mathbf{r}_o)$ an arbitrary Gaussian function was used, which can be applied for any SMB because its DSC is such that $\widetilde{\gamma}_m(\mathbf{r}_o)$ is a real-positive function. Applying this algorithm the object wavefield and the DSC can be successfully recovered from the experimental data [24]. We recall that the DSC, $\gamma(\mathbf{r}) = FT^{-1}[\widetilde{\gamma}_m](\mathbf{r}S_m^{-1})$, is obtained in the input plane of the setup.

The root-mean-square (RMS) error between reconstructed and measured constraint images allows for monitoring the algorithm convergence as well as estimating the accuracy of the reconstructed object wavefield. Here, we have considered the normalized RMS error (ε) given by: $\varepsilon^2 = \sum_{q=1}^{Q} \left[\sqrt{c_q'} - \sqrt{c_q} \right]^2 / \sum_{q=1}^{Q} c_q$, where $c_q' = \Im_{PC}^{(m,n)}(q)$, $c_q = I_{PC}^{(m)}(q)$, with q being the pixel index and Q the number of pixels of the image. In the experiments described in the following Sections, the algorithm reached convergence with low RMS error (below 15 %) after few iterations (typically $N = 10$ and $K = 2$, for $M = 9$).

The Fresnel diffraction integral [Eq. (2)] is numerically calculated using the angular spectrum decomposition method, see for example [3, 27]. The described iterative algorithm reached convergence within a minute (Intel Core i7 CPU and Matlab R2013a, with images of $Q = 1024 \times 1024$ pixels). Nevertheless, to speed up the MI reconstruction, the computation was preformed using a Graphics Processing Unit (GPU, nVidia GeForce GTX550-Ti), thus reconstructing the object wavefield $f(\mathbf{r})$ and DSC in few seconds (typically 20 s).

3. Experimental setup and testing results

In this Section we demonstrate that the described technique is well-suited for quantitative phase imaging in microscopy with fully or partially coherent light illumination. Two alternative kinds of illumination sources are considered: Laser (Qioptiq, iFLEX-Gemini, $\lambda_{laser} = 640 \pm 1$ nm, coherence length ~ 5 mm) and LED (Kingbright, GaAlAs, $\lambda_0 = 648 \pm 1$ nm, $\Delta\lambda = 12 \pm 2$ nm corresponding to coherence length $\sim 17\,\mu$m in water), which provide fully and partially temporal-spatial coherent illumination over the sample, correspondingly. In the transmission inverted microscope sketched in Fig. 1(b), the sample is enclosed between two glass coverslips (attached with a double-sided tape $\sim 90\,\mu$m thick, glass thickness 0.17 mm) and imaged under Köhler illumination by an oil immersion objective (Olympus UPLSAPO, 1.4 NA, 100×, oil Cargille Type B). As a condenser we used a 10× objective (Nikon Plan Achromat, 0.25 NA).

In this setup the ETL (Optotune, EL-10-30-C) yields a tunable focusing scan of the sample and the resulting imaged planes are acquired by a high-speed sCMOS camera (Hamamatsu, Orca Flash 4.0, 16-bit gray-level, pixel size of 6.5 μm). The shift of the imaged plane is given as a function of the focal length (f) of the ETL, the effective magnification of the objective-tube lenses ($M = 83$) and focal length f_{RL} of the relay lens as it follows: $\triangle z = n_s f_{RL}^2 (f - d)/fdM^2$, where $n_s = 1.33$ is the refractive index of the immersion medium (water). The focal range of the ETL is $84 - 208$ mm and therefore the available focusing scan range is about 30 μm. Nevertheless, the measurement of the constraint images is performed in a shorter focusing scan range (15 μm) according to the coherence gating of the LED illumination. As previously discussed, the proposed MI recovery technique reconstructs the object wavefield only within the coherence gate defined by the longitudinal coherence length of the LED. To avoid distortions in the reconstructed information (e.g. object's phase and DSC) caused by the Brownian motion in the sample, the acquisition of the constraint images (1024 × 1024 pixels) was performed in
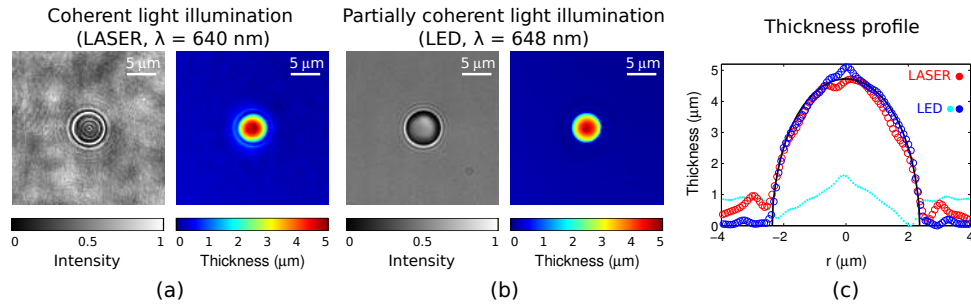
Fig. 2. Measured images of a polystyrene bead and its thickness reconstruction using coherent laser (a) and partially coherent LED (b) illumination sources. (c) Thickness profile of a spherical bead (black line plot) and the reconstructed ones for laser and LED (red and blue scatter plots). The phase retrieval algorithm fails to reconstruct the thickness when the partial coherence of the LED is ignored, see cyan colored dotted-line plot in (c).

about 125 ms at 144 frames per second (fps). This was achieved by using a periodic current driving signal of 2 Hz (triangular, current range $0 - 293$ mA) applied to the ETL. Although 18 images are acquired in 125 ms, we considered only the nine ones belonging to the coherence gate. The corresponding focal lengths are: 122.4, 115.7, 109.9, 104.6, 100.0, 95.8, 91.8, 87.9 and 84.3 mm (range $140 - 293$ mA, see Appendix). Note that the ETL can be set up to 10 Hz for faster measurement that requires high frame rate acquisition above 200 fps. In our case an electrical lens driver controller with 12-bit precision for current and frequency control has been used. Both sCMOS camera and ETL were controlled with a Labview program developed by us.

To test the technique, let us first consider the reconstruction of the thickness distribution of polystyrene spheres diluted in distilled water (4.7μm bead diameter, Spherotech Lot. AD01) using laser ($n_o(640\,\text{nm}) = 1.587$) and LED ($n_o(648\,\text{nm}) = 1.586$) illumination. From the retrieved phase $\phi(\mathbf{r})$ of the object wavefield, the particle thickness $t(\mathbf{r})$ is determined as it follows: $t(\mathbf{r}) = \phi(\mathbf{r})\lambda_0/2\pi\triangle n$, where $\triangle n = n_o - n_s$ is the refractive index difference between the bead (n_o) and its surrounding medium (water, $n_s = 1.33$) [3, 4]. For accurate phase unwrapping we applied the algorithm reported in [28]. The measured image of the best focused bead and the reconstructed thickness distribution are shown for each illumination case in Fig. 2(a) and 2(b), respectively. These results are in good agreement with the expected thickness profile of a spherical bead, as displayed in Fig. 2(c). Specifically, the diameter of the bead is $4.8 \pm 0.1 \mu$m. The reconstruction of the object wavefield completely fails [see thickness profile plotted by a cyan dotted-line in Fig. 2(c)] when the LED illumination is incorrectly assumed as fully spatial coherent. These facts prove that for accurate quantitative imaging the spatial coherence of the illumination has to be taken into account.

Both fully and partially coherent illumination can be used for phase imaging, however, partial coherence brings relevant advantages. As observed in Fig. 2(a), coherent laser illumination yields multiple reflections and interference (mostly caused by coverslip glasses, surrounding media, etc.) degrading the image. While, in the case of LED illumination the object's image exhibits uniform background with suppressed noise, see Fig. 2(b) and 2(c). This kind of noise reduction have also been exploited in digital holographic microscopy with LED sources, see [15, 16].

The advantages of partially coherent light are more relevant with samples exhibiting multiple layers, e.g. blood smears, biofilms and scattering media. To illustrate this fact, let us consider as an example a scattering media that consists of a layer of polystyrene beads fixed over the top coverslip as sketched in Fig. 3. In the case of coherent laser illumination, the beam is scat-
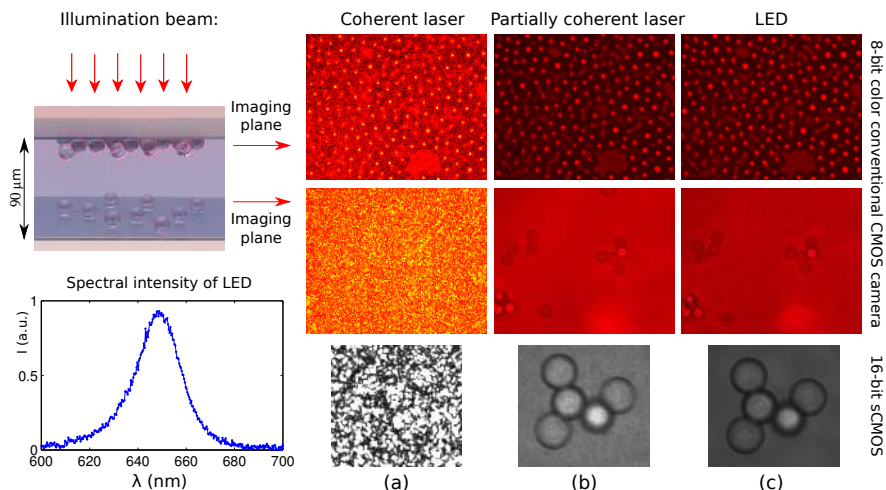
Fig. 3. Left panel: Sketch of the sample (scattering media on the top coverslip) illuminated by a monochromatic laser beam and quasi-monochromatic partially coherent LED beam. The measured power spectrum of LED ($\lambda_0 = 648 \pm 1$ nm, $\Delta\lambda = 12 \pm 2$ nm) is displayed. Right panel: (a)-(c) Images of the sample at the chamber's top and bottom coverslips, for each illumination case. Images acquired by the high-resolution sCMOS camera are displayed at the third row as a zoom inset.

tered by the layered structure yielding speckle noise in the image Fig. 3(a). In contrast, the speckle noise is mitigated when using a partially coherent laser and LED beams as shown in Fig. 3(b) and 3(c), respectively. The laser beam with low spatial coherence was generated by using a moving diffuser (Optotune, LSR-3005-12D-VIS), [23, 24]. Note that the LED beam is both temporal and spatial partially coherent. Its coherent length in the sample medium (water) is $\sim 17\,\mu$m, which was estimated from the measured power spectrum of the LED displayed in Fig. 3. In spite of the difference in the temporal coherence, the images of the particles at the chamber's top and bottom are similar in both cases [see second row of Fig. 3(b) and 3(c)], when acquired by a conventional CMOS camera (exposure time of 60 ms, Thorlabs-DCC1240C). This demonstrates that low spatial coherence allows for speckle noise suppression. Nevertheless, in high-speed measurement the image [see third row of Fig. 3(b) and 3(c)] is completely free of speckle noise only under the LED illumination. A small amount of speckle noise persists in Fig. 3(b) due to the limited refresh rate of the time-varying diffuser with respect to the short acquisition rate of the sCMOS camera (10 ms in this case). Therefore, LED illumination is preferable for coherent noise suppression in high-speed measurements.

The latter examples underline the importance of the partial coherence for speckle noise reduction in the image and the optical sectioning capabilities. In the next section, we experimentally demonstrate that spatial coherence properties of quasi-monochromatic LEDs are also crucial to obtain accurate quantitative phase imaging of biological samples such as blood smears.

4. Quantitative phase imaging of biological specimens with partially coherent light

In vivo analysis of blood smears reveals important information for clinical studies. Quantitative phase imaging is a powerful tool for maker-free microscopy that has been extensively applied for analysis of red blood cells (RBCs) immersed in different environments [11, 12]. Here, we consider human blood smear (without staining) which has heterogeneous cell distribution structured in several layers over the sample. This is a realistic example to study the benefits of
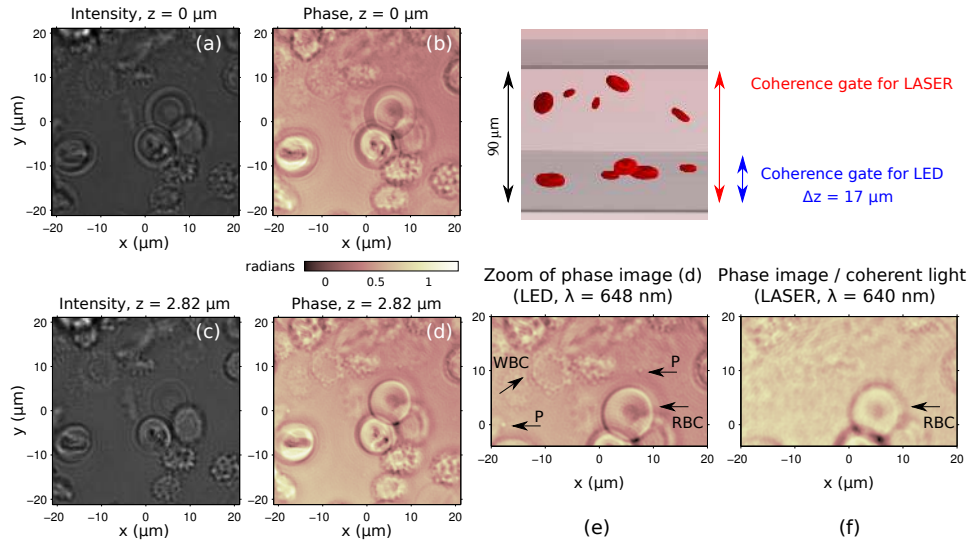
Fig. 4. (a)-(d) Intensity and phase of the reconstructed object wavefield at different focusing planes. RBCs, WBCs and platelets (P) are distinguished in the phase images (d) and (e). Coherent laser illumination yields significant cross-talk degrading the phase image (f).

partially coherent light for quantitative phase imaging of living biological specimens.

As in the previous experiments discussed in Section 3, the sample was enclosed between two glass coverslips and the measurement was performed at 144 fps to avoid motion artifacts in the reconstruction, see Media 1. Here, we also used nine constraint images to reconstruct both the object wavefield and the DSC. Figures 4(a) and 4(b) show the intensity and phase of the retrieved object wavefield at the focusing plane $z = 0$. We underline that the reconstructed object wavefield can be numerically refocused within the coherence gate, which is crucial in the analysis of the sample. Indeed, both RBCs and white blood cells (WBCs) can be accurately focused by numerical propagation of the object wavefield, as observed in Fig. 4(c) and 4(d) for $z = 2.82\,\mu$m. In contrast to the intensity image, these cells are clearly distinguished in the phase image Fig. 4(d). Moreover, small cell structures and platelets ($2-3\,\mu$m in diameter) are observed as indicated in the zoom inset Fig. 4(e). These structures, however, are washed out in the phase image obtained with the coherent laser illumination Fig. 4(f). Indeed, the overall image quality is significantly degraded and only RBCs are distinguished.

The accuracy of the object wavefield reconstruction can be estimated by the RMS error between the measured constraint images and the ones calculated from the retrieved information (DSC and object wavefield), see Fig. 5(a). In the case of LED illumination the algorithm reached convergence with RMS error about 12 %. This low value of RMS error demonstrates high accuracy in the reconstruction of both the object wavefield and the DSC. As in the testing experiments discussed in Section 3, the DSC amplitude [see Fig. 5(b)] fits well to the Gaussian function $|\gamma(\triangle \mathbf{r})| = \exp(-|\triangle \mathbf{r}|^2/2\sigma^2)$ with $\sigma = 4.8\,\mu$m, which is often referred to as lateral coherent length or spatial coherence radius.

For coherent illumination the object wavefield was reconstructed with a RMS error about 15%, however, the cells in the retrieved phase [Fig. 4(f)] are barely distinguished in comparison to the partially coherent case [Fig. 4(e)]. This degradation in the phase image is caused by the cross-talk arising from the light scattered by different objects (mostly RBCs and WBCs) distributed in volume.

The temporal and spatial partial coherence of LED illumination work together to significantly
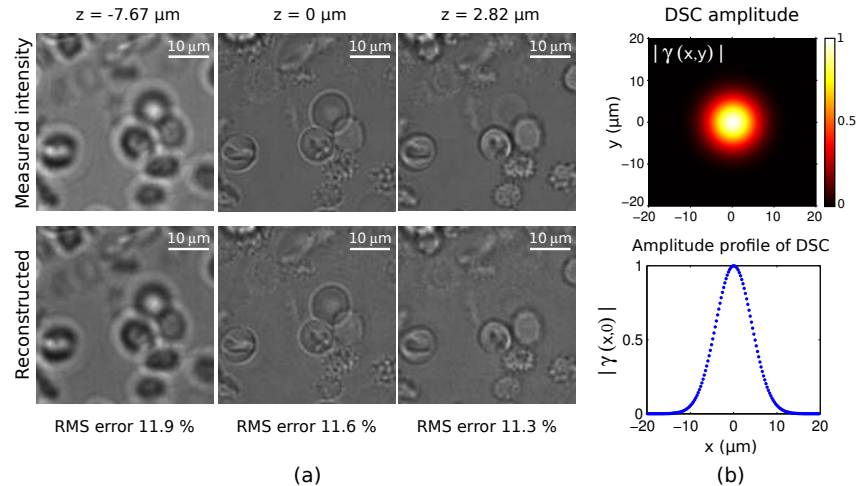
Fig. 5. (a) Measured constraint images and the reconstructed ones with RMS error about 12 %. The measured stack of images is provided as video file in Media 1 to illustrate the high-speed acquisition. (b) Amplitude of the reconstructed DSC and its 1D profile.

mitigate the cross-talk. We recall that the reduced temporal coherence mostly prevent from interference caused by light scattered by objects distributed in volume (axial sectioning). While the limited spatial coherence mostly contributes to cross-talk reduction in transverse planes. A detailed description of the interplay between temporal and spatial coherence effects needs further research. In the case of multi-layered samples, the use of narrow-band partial coherent illumination and high-NA objectives has been demonstrated powerful for high resolution imaging with interference microscopy [20]. The proposed technique paves another way to exploit the spatial coherence in this context. Although the studied blood smear consists of few layers, the quantitative phase images obtained with partially coherent light exhibit higher resolution than the coherent ones.

5. Discussion

The proposed non-interferometric iterative technique reconstructs, *in-situ*, both the object wavefield and degree of spatial coherence of the illumination beam. Its optical implementation is straightforward in conventional microscopes at low cost, without altering the microscope design. In general, it can be combined with digital image processing methods which, for example, take into account the point spread function of the microscope.

We have experimentally demonstrated accurate quantitative phase imaging with partially coherent illumination. It requires the knowledge of the degree of spatial coherence that, in the proposed technique, is determined from the same measured data as used for the object wavefield recovery. The reconstructed phase images are free of speckle noise and exhibit higher resolution than in the coherent case for samples comprising several layers such as blood smears. The measurements were performed in the millisecond range and the object wavefield was reconstructed in a few seconds, that is well-suited for real-life applications.

Light sources with the spatial coherence tailored [13, 14] to a particular imaging application may provide an additional advantage to the proposed technique. We underline that as the spatial coherence becomes low the measurement defocusing range has to be shorter. In this range the object's diffraction patterns have to be well resolved and vary with defocus such that the algorithm can recover the phase information. This fact has also been pointed out in [24, 29],

where further information about the domain of applicability is discussed.

Appendix

A1. Intensity distribution of a partially coherent SMB at the output of the ABCD system

The beam propagation through the measurement system discussed in Section 2, Fig. 1(a), is described in paraxial approximation by the ABCD transform $\mathscr{F}^{(m)}$. This transformation can be easily calculated by using the ray transfer matrix [30] of the setup comprising the RL (fixed focal length f_{RL}) and ETL (variable focal length f_m). Specifically, it is given by

$$\mathscr{F}^{(m)}\left[f\left(\mathbf{r}_i\right)\right]\left(\mathbf{r}_o\right) = \int f\left(\mathbf{r}_i\right) K^{(m)}\left(\mathbf{r}_i, \mathbf{r}_o\right) d\mathbf{r}_i, \tag{5}$$

where the kernel is

$$K^{(m)}\left(\mathbf{r}_i, \mathbf{r}_o\right) = \sigma\beta_1 \exp\left[i\pi\sigma\left(-2\mathbf{r}_i\mathbf{r}_o\beta_1 + \mathbf{r}_i^2\beta_2 + \mathbf{r}_o^2\beta_3\right)\right],$$

with: $\sigma = 1/\lambda f_{RL}$, $\beta_1 = f_m/(d - f_m)$, $\beta_2 = -\beta_1 f_{RL}/f_m$ and $\beta_3 = -\beta_1 d/f_m$.

In the case of the partially coherent light, with $\Gamma(\mathbf{r}_1, \mathbf{r}_2)$ at the input plane of the system, the intensity distribution at its output plane is expressed as it follows:

$$I_{PC}^{(m)}\left(\mathbf{r}_o\right) = \iint \Gamma\left(\mathbf{r}_1, \mathbf{r}_2\right) K^{(m)}\left(\mathbf{r}_1, \mathbf{r}_o\right) K^{*(m)}\left(\mathbf{r}_2, \mathbf{r}_o\right) d\mathbf{r}_1 d\mathbf{r}_2, \tag{6}$$

Taking into account that the beam is described by the Schell model and introducing new variables, $\triangle\mathbf{r} = \mathbf{r}_1 - \mathbf{r}_2$ and $\mathbf{R} = (\mathbf{r}_1 + \mathbf{r}_2)/2$, the Eq. (6) is expressed as

$$\begin{aligned}I_{PC}^{(m)}\left(\mathbf{r}_o\right) = \ & (\sigma\beta_1)^2 \iint f\left(\mathbf{R} + \frac{\triangle\mathbf{r}}{2}\right) f^*\left(\mathbf{R} - \frac{\triangle\mathbf{r}}{2}\right) \exp\left[i2\pi\sigma\beta_1\left(Xx + Yy\right)\right] d\mathbf{R} \\ & \times \ \gamma(\triangle\mathbf{r}) \exp\left[i2\pi\sigma\beta_1\left(x_o x + y_o y\right)\right] d\triangle\mathbf{r}.\end{aligned} \tag{7}$$

Since for the coherent case the intensity $I_C^{(m)}(\mathbf{r}_o)$ is also obtained from the latter expression with $\gamma(\triangle\mathbf{r}) = 1$, one can rewrite Eq. (7) as a convolution:

$$I_{PC}^{(m)}\left(\mathbf{r}_o\right) = I_C^{(m)}\left(\mathbf{r}_o\right) \otimes \widetilde{\gamma}_m\left(\mathbf{r}_o\right) = \int I_C^{(m)}\left(\mathbf{r}'_o\right) \widetilde{\gamma}_m\left(\mathbf{r}_o - \mathbf{r}'_o\right) d\mathbf{r}'_o, \tag{8}$$

where $\widetilde{\gamma}_m(\mathbf{r}_o)$ is the scaled FT of the input DSC: $\widetilde{\gamma}_m(\mathbf{r}_o) = FT\left[\gamma(\triangle\mathbf{r})\right](\mathbf{r}_o\beta_1)$. This fact has been found for other ABCD systems in [19, 24, 26] as well. Note that the $FT[\cdot]$ is optically performed by RL.

A2. Calibration data of the ETL and its paraxial approximation

In our case, the electrically tunable lens (Optotune EL-10-30-C) is made from a low dispersion and polarization preserving material with refractive index $n_{lens} = 1.299$. It has a plano-convex shape that is accurately controlled in the focal tuning range $84 - 208$ mm. We assume that the ETL can be described by the transmission function

$$T(\mathbf{r}) = \exp\left(i2\pi(\rho \cdot (n_{lens} - 1) + \rho_0)/\lambda\right), \tag{9}$$

where its parabolic shape is given by

$$\rho = \sqrt{\left(\frac{\rho_0}{2} + \frac{a^2}{2\rho_0}\right)^2 - r^2} + \frac{\rho_0}{2} - \frac{a^2}{2\rho_0}, \tag{10}$$
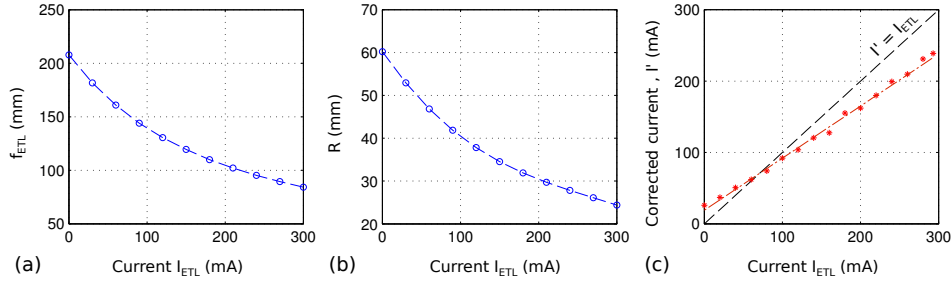
Fig. 6. (a) Calibration functions for the back focal length of the ETL and (b) for its radius of curvature. (c) Correction function for the current (red line) and experimental data (red scatter plot).

with ρ_0 being the central deflection of the lens, $a = 5.5$ mm is the semi-diameter of the lens and $r^2 = x^2 + y^2$. The parameter ρ_0 is a function of the applied current I_{ETL} (range $0 - 293$ mA). Expression Eq. (10) and a Zemax model of the ETL were provided by the manufacturer.

To deal with the paraxial approximation, the expression Eq. (10) is written as a series expansion at first order: $\sqrt{b^2 - r^2} \simeq b - r^2/2b$, where $b = (\rho_0^2 + a^2)/2\rho_0$. Therefore, the transmission function of the thin tunable lens is given by

$$L(\mathbf{r}) = \exp\left(-i\pi r^2/\lambda \mathrm{f}\right) \exp\left(i2\pi\rho_0 n_{lens}/\lambda\right), \qquad (11)$$

where its focal length f is a function of ρ_0 and thus of the applied current:

$$\mathrm{f}(\rho_0) = \frac{\rho_0^2 + a^2}{2\rho_0(n_{lens} - 1)}. \qquad (12)$$

The term $\exp\left(i2\pi\rho_0 n_{lens}/\lambda\right)$ in Eq. (11) yields a variable phase shift with $\rho_0 = \rho_0(I_{ETL})$.

To calibrate the focal length of the thin tunable lens, the function $\rho_0(I_{ETL})$ has to be determined. The back focal length of the ETL (f_{ETL}) is given as a function of I_{ETL} as displayed in Fig. 6(a), according to the manufacturer's data. Note that the Zemax model of the ETL allows for estimation of both f_{ETL} and the corresponding radius of curvature (R). Since the central deflection of the lens is $\rho_0 = R - \sqrt{R^2 - a^2}$, the values $\rho_0(I_{ETL})$ can be estimated from $R(f_{ETL})$ taking into account the calibration $f_{ETL}(I_{ETL})$, see Fig. 6(b). In our case, $\rho_0 \in [0.25, 0.55]$ mm and the ETL is well approximated by the thin tunable lens, Eq. (11), when using a *correction function* of the current for the expression Eq. (12). This correction takes into account the effects of variable thickness of the real ETL in such a way that the thin lens behaves as a calibrated virtual ETL in the iterative algorithm. In Fig. 6(c) this correction function ($I' = 0.73 I_{ETL} + 19.1$ mA) is plotted as a function of the applied current I_{ETL}. It has been estimated by linear fitting of the focal length shift of the uncorrected thin lens with respect the measured values f_{ETL}. The calibrated focal length values used in the measurement (see Section 3) correspond to the current values: 140, 160, 180, 200, 220, 240, 260, 280 and 293 mA.

Finally, we underline that coma aberration caused by gravity (about 0.21λ RMS, in the 80 % of ETL's central aperture) can be included in this lens model to prevent distortions in the reconstructed image. Nevertheless, in the proposed setup [Fig. 1(b)] the object wavefield is focused into the ETL and thus illuminates the central region (about 40 % of the aperture) where such a phase aberration can be neglected.

Acknowledgments